The Mechanism of Creep in Gamma Prime Precipitation-Hardened Nickel-Base Alloys at Intermediate Temperatures

GERALD R. LEVERANT AND BERNARD H. KEAR

The creep deformation of Mar-M200 single crystals of various orientations has been studied at a temperature of 1400°F. It was found by a combination of transmission microscopy and analysis of lattice rotations that shear of the γ-γ' structure occurs by the glide of loosely coupled intrinsic/extrinsic fault pairs with a net Burgers vector of $a\langle 112\rangle$. The orientation dependencies of both the rate and extent of primary creep are correlated with the Schmid factors and multiplicity of slip for $\{111\}\langle 112\rangle$ systems. It is also shown that strain hardening due to intersecting slip is necessary to obtain the transition from primary to steady-state creep. In addition, it was found that the deformation mode is a function of strain rate at 1400°F. In contrast to the observed glide mechanism during creep, tensile deformation occurs by the shear of the γ and γ' phases by $a/2\langle 110\rangle$ superlattice pairs.

PRECIPITATION-hardened nickel-base alloys have found useful application in gas turbine engines primarily because of their excellent elevated temperature creep resistance. Research on the creep behavior of these materials has been mainly confined to grain boundary phenomena,[1-6] and overall phenomological behavior,[7-12] with virtually no attempts having been made to understand fundamental creep deformation mechanisms and their implications. The recent development of casting techniques[13] that yield single crystals of these materials has provided an opportunity to investigate these mechanisms in detail.

In this study, single crystals of Mar-M200 of various orientations have been crept at a single temperature and a single stress to determine the orientation dependence of creep behavior, and transmission electron microscopy has been combined with these observations to elucidate the creep mechanism.

I) MATERIAL AND EXPERIMENTAL PROCEDURE

Several different heats of material were cast for this investigation. Close control was maintained over the composition of these heats, Table I, particularly with respect to aluminum, titanium, and niobium (columbium) which control the amount and strength of the γ' precipitate. Carbon was maintained at a low level by not making deliberate additions of it to the melt. This prevented the formation of MC carbides and greatly reduced the number of $M_{23}C_6$ carbides.

After casting, all crystals were solutionized in argon at 2250°F for 100 hr and air cooled. They were then aged at 1600°F for 32 hr and air cooled which resulted in the structure shown in Fig. 1. The ordered fcc γ' particles are cuboidal with rounded corners, ~0.25 μ on edge, and coherent with the disordered fcc γ matrix. The composition and volume fraction of the γ' particles from three different heats is shown in Table II. These determinations were made by a recently developed extraction technique,[14] and the reported values for the three different single crystal heats indicate the excellent heat-to-heat reproducibility. The amount of γ'-forming elements (titanium, aluminum, niobium) in these heats covered most of the range for these elements shown in Table I.

The orientation of each machined creep specimen was determined by the Laue back-reflection X-ray technique by placing the specimen in a fixture designed to align the specimen axis parallel to the X-ray beam. Reported orientations have an accuracy of ±1.5 deg. The specimens used in this investigation were identical to a previous design.[15] An extensometer was attached to ridges at the extremes of the gage section and strain was measured by an LVDT. Most tests were performed at a stress of 100 ksi and temperature of 1400°F in constant load creep machines. The temperature was maintained to within ±2°F over the 1.5

Table I. Analyzed Compositional Range of Mar-M200 Single Crystals

Al	4.5 to 4.8 wt pct
Co	9.8 to 11.3
Cr	8.5 to 9.4
Nb	0.51 to 0.71
Ti	1.5 to 1.8
W	11.4 to 12.3
B	0.003 to 0.019
Zr	0.032 to 0.051
C	~50 ppm

Table II. Composition and Volume Fraction of γ' in Three Single Crystal Heats

		Wt Pct						
Heat	Vol Pct, γ'	Al	Co	Cr	Nb	Ni	Ti	W
X4C	57.1	6.8	6.2	2.39	1.11	67.9	2.28	13.3
X4K	58.4	6.7	6.2	2.37	1.05	67.8	2.29	13.5
X4W	56.5	6.8	6.3	2.38	1.04	67.5	2.28	13.7

GERALD R. LEVERANT and BERNARD H. KEAR are Senior Research Associate and Metallurgist, respectively, Advanced Materials Research and Development Laboratory, Pratt & Whitney Aircraft, Middletown, Conn.

Manuscript submitted July 2, 1969.

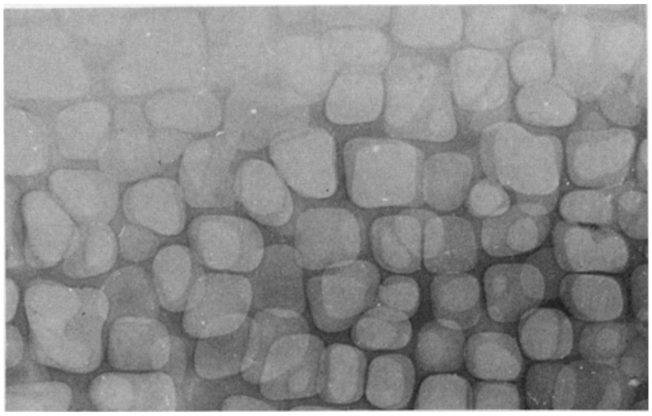

Fig. 1—A transmission micrograph of the γ-γ' structure of heat-treated Mar-M200. Magnification 29,000 times.

in. gage length. Most specimens were run to failure (~200 hr) while others, from which thin foils for transmission microscopy were taken, were forced-air cooled under load to room temperature at various stages in primary and steady-state creep.

Thin foils were prepared by an established procedure.[16] The polishing solution used for final thinning consisted of 83 pct methanol, 7.5 pct sulfuric acid, 3 pct nitric acid, 2 pct hydrofluoric acid, and 4.5 pct lactic acid. Polishing was performed at room temperature and 10 v.

II) EXPERIMENTAL RESULTS

A) Characterization of Creep Behavior. The orientations of the tensile axes of the single crystals tested are shown in Fig. 2. All specimens are within 18 deg of [001] with the exception of crystal 1. Some creep curves are shown in Fig. 3(*a*). The curves for crystals 6 and 13 are typical for most orientations tested, exhibiting an incubation period and regions of primary, steady-state, and tertiary creep. The slope of the linear portion of the primary creep region is defined as the primary creep rate, Fig. 4. The creep curve for crystal 1 is not typical, exhibiting no transition to steady-state creep prior to failure, Fig. 3(*b*).

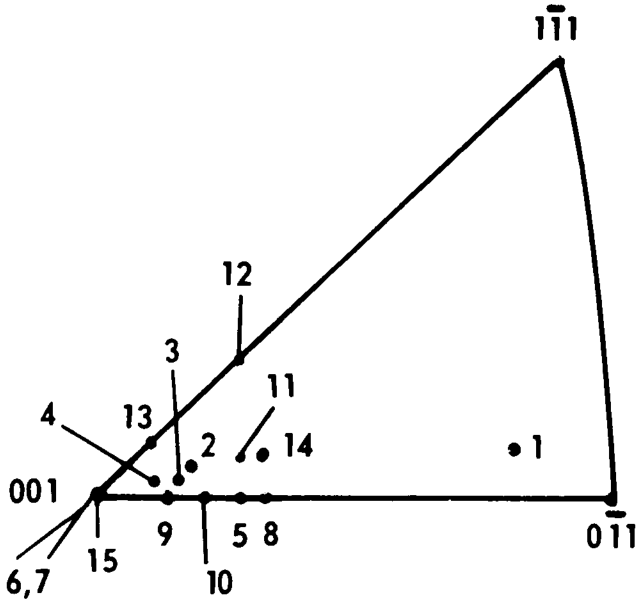

Fig. 2—The initial orientation of the tensile axes of the single crystals in the standard stereographic triangle.

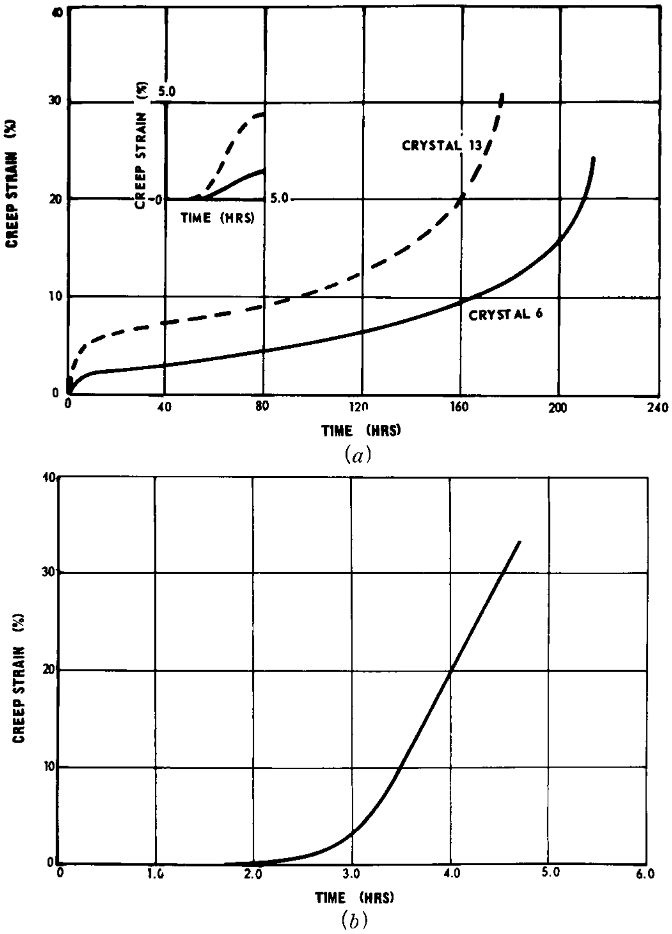

(*a*)

(*b*)

Fig. 3—(*a*) The creep curves for crystals 6 and 13. The inset shows the initial portion of the creep curves including the incubation period. (*b*) Creep curve for crystal 1.

Table III summarizes the creep data for all crystals including the primary creep strain (ϵ_p in Fig. 4), primary creep rate ($\dot{\epsilon}_p$), steady-state creep rate ($\dot{\epsilon}_s$), and the ratio of primary to steady-state creep rates.

Table III. Creep Data

Crystal No.	Stress, ksi	Primary Creep Strain, Pct	Primary Creep Rate ($\dot{\epsilon}_p$) X 10^{-2}, hr^{-1}	Steady-State Creep Rate ($\dot{\epsilon}_s$) X 10^{-4}, hr^{-1}	$\dot{\epsilon}_p/\dot{\epsilon}_s$
1	100	Unconventional creep curve, Fig. 3(*b*)			
2	100	5.5	1.96	4.20	46.7
3	100	4.5	1.49	2.82	52.9
4	100	3.3	0.975	3.40	28.7
5	89.2	1.5	0.105	0.62	16.9
6	100	1.7	0.610	3.52	17.3
7	100	1.9	0.555	3.06	18.1
8	100	2.2	0.553	–	–
9	100	2.4	1.02	4.77	21.4
10	100	4.0	1.52	3.40	44.7
11	85.5	Test stopped in primary creep at 1.4 pct strain.			
12	100	12.5	5.60	12.5	44.8
13	100	5.2	2.07	5.05	41.0
14	100	6.3	1.60	4.53	35.4
15	85.0	0.8	0.0516	0.348	14.8

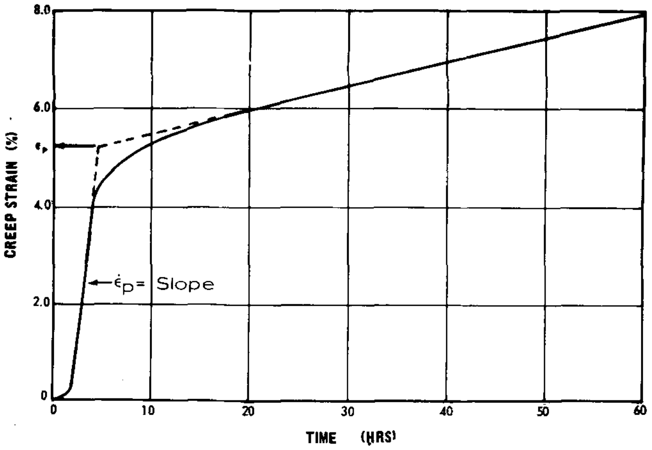

Fig. 4—The definition of the primary creep strain (ϵ_p) and the primary creep rate $(\dot{\epsilon}_p)$ shown on the creep curve for crystal 13.

For the tests run at 100 ksi, the primary creep strain and primary creep rate increase progressively with orientation in the following order: [001] tensile axis, tensile axis on $[001]$-$[0\bar{1}1]$ boundary, tensile axis between $[001]$-$[0\bar{1}1]$ and $[001]$-$[1\bar{1}1]$ boundaries, and tensile axis on $[001]$-$[1\bar{1}1]$ boundary. The steady-state creep rate increases with orientation in the same order as the primary creep rate but does not exhibit as large a spread as the primary rate. This is more clearly seen by comparing the ratio of primary creep rate to steady-state creep rate. The ratio increases from about 18 for a [001] orientation to 45 to 50 for certain orientations removed from [001]. This ratio would have been even higher for specimens experiencing large primary strains if the tests had been conducted under constant stress rather than constant load, because $\dot{\epsilon}_s$ would have been considerably reduced. Attempts to rationalize the orientation dependence of the extent and rate of primary creep by consideration of the Schmid factors (S.F.) and multiplicity of slip for assumed $\{111\}\langle 110\rangle$ slip systems proved fruitless. This can be seen most clearly by comparing the primary creep rates of crystals 6 through 10 on the $[001]$-$[0\bar{1}1]$ boundary line with the Schmid factor for $(\bar{1}\bar{1}1)[101]$ slip for each crystal. As the orientation deviated from [001], the primary creep rate initially increased, passed through a maximum, and then decreased, whereas the S.F. continually increased, Fig. 5(*a*). Identification of the actual slip systems was then undertaken.

B) Identification of Operative Slip Systems During Creep. Most details of the analysis performed to identify the operative slip system have been described.[17] Here, only the salient features of that analysis are given and some additional observations are included as well. Fig. 6(*a*) shows the dislocation structure in crystal 11 in primary creep at a strain of 1.4 pct; the plane of the foil is normal to the tensile axis. Slip-induced stacking faults can be seen on two different planes. The slip planes were identified as $\{111\}$ by comparing a similar micrograph containing stacking faults on three different planes with a stereographic projection of the $\{111\}$ slip traces in the plane of the foil. It was found that most stacking faults in this foil were parallel to the critical plane, $(1\bar{1}1)$, rather than the normally expected primary plane $(\bar{1}\bar{1}1)$. Foils were then prepared parallel to both $(1\bar{1}1)$ and $(\bar{1}\bar{1}1)$. A relatively high density of very long dislocations was found in the critical plane $(1\bar{1}1)$, but virtually no dislocations were seen in the primary plane $(\bar{1}\bar{1}1)$ confirming the trace analysis.

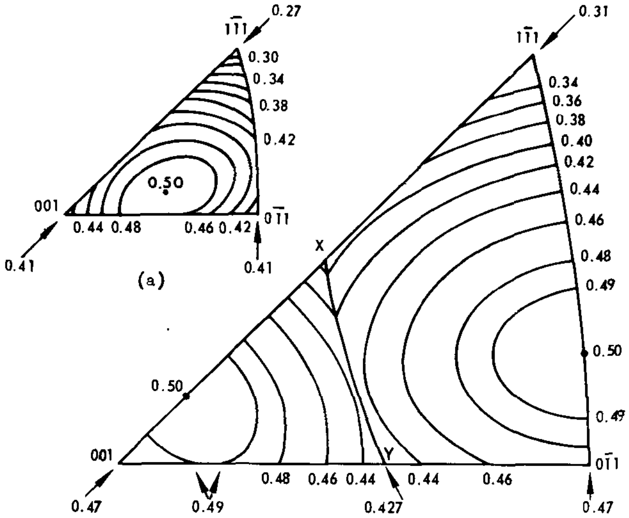

Fig. 5—Schmid factor contours for the most highly stressed (*a*) $\{111\}\langle 110\rangle$ slip system, (*b*) $\{111\}\langle 112\rangle$ slip system.

An example of the dislocation structure in the critical plane is shown in Fig. 7. The dislocations are shearing the γ' particles as loosely coupled pairs associated with intrinsic and extrinsic stacking faults. For example, the stacking fault between dislocations 1 and 2 is intrinsic and between 3 and 4 is extrinsic. Dislocations 1 and 4 in Fig. 7 have Burgers vectors of $a/3\langle 112\rangle$, and dislocations 2 and 3 have Burgers vectors of $a/6\langle 112\rangle$.[17] The dislocations are all of the same sign and, therefore, the net Burgers vector of the pair is $a\langle 112\rangle$. In addition to the dislocations with $a/3\langle 112\rangle$ and $a/6\langle 112\rangle$ Burgers vectors, some dislocations with $a/2\langle 110\rangle$ Burgers vectors were also observed.

In order to demonstrate convincingly that the $a\langle 112\rangle$ dislocations were primarily responsible for the creep deformation, the lattice rotation of several crystals was determined after failure, Fig. 8. The most highly stressed slip system for crystals 12, 13, and 14 was $(1\bar{1}1)[\bar{1}12]$, and the crystals rotated cirectly toward $[\bar{1}12]$. In the case of crystal 1, the direction of rotation was toward $[2\bar{1}1]$ which is the slip direction in the most highly stressed slip system, $(\bar{1}\bar{1}1)[2\bar{1}1]$, for this orientation. Since lattice rotation in single crystals tends toward the slip direction,[18] this confirmed that the dislocations with net Burgers vector of a $\langle 112\rangle$ were responsible for creep deformation. In addition to the above results, crystal 5 rotated along the $[001]$-$[0\bar{1}1]$ boundary toward [001] which is consistent with equal slip activity on the $(1\bar{1}1)[\bar{1}12]$ and $(\bar{1}\bar{1}1)[112]$ systems, and crystals with a [001] tensile axis were stable, indicating equal activity on all four equally stressed slip systems.

C) Activation Energy for Creep. Activation energies were measured during steady-state creep by the temperature cycling method.[19] The results are summarized in Table IV; all values for activation energy (ΔH) are the average of 6 to 7 determinations. The measured values of ~150 kcal per mole were inde-

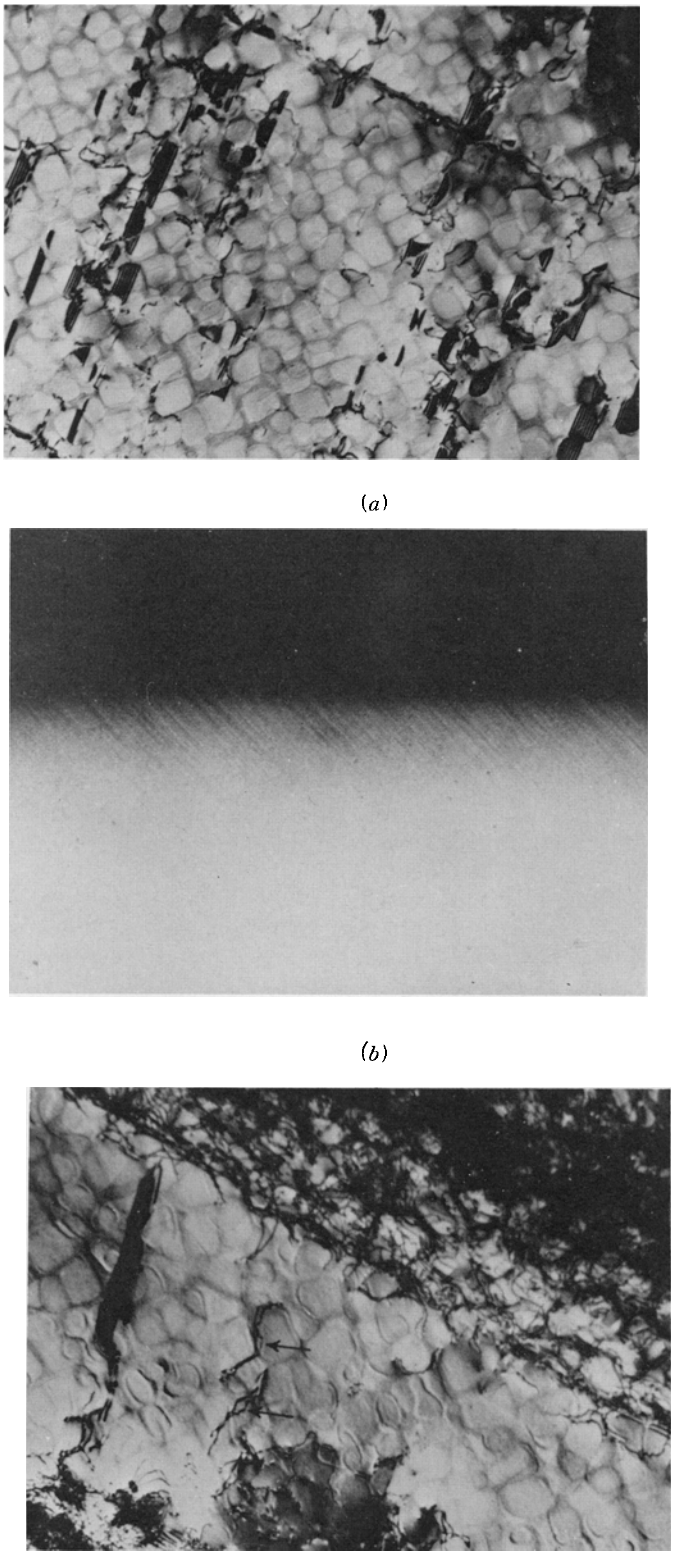

(a)

(b)

(c)

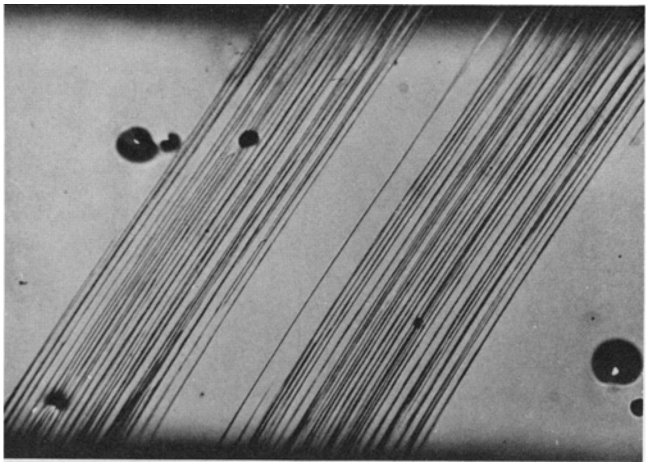

(d)

Fig. 6—(a) Transmission micrograph showing intrinsic/extrinsic fault pairs (arrows) in crystal 11 at 1.4 pct strain in primary creep. Magnification 16,800 times. (b) Uniform distribution of surface slip offsets in specimen crept to 1.5 pct strain in primary creep. Magnification 95 times. (c) Transmission micrograph of tensile specimen at 1.8 pct strain showing intense slip band and $a/2\langle 110\rangle$ superlattice pairs (arrows). Magnification 21,200 times. (d) Surface offsets showing the heterogeneous nature of tensile deformation at 1400°F. Magnification 95 times.

pendent of stress and crystal orientation. In addition, it was observed that ΔH was independent of strain.

D) Effect of Strain Rate on Slip Character and Slip Systems. Creep-induced deformation was quite homogeneous as is evident from the uniform distribution of dislocations shown in Fig. 6(a) and the surface slip offsets, Fig. 6(b). In contrast, the deformation produced during tensile testing at 1400°F and a strain rate of 2.0 per hr was extremely heterogeneous, Figs. 6(c) and (d), and occurred by the motion of superlattice pairs in intense bands as has been observed at room temperature for this material.[20] The pairs at 1400°F were identified as $a/2\langle 110\rangle$ dislocations by the $\bar{g}.\bar{b}. = 0$ criterion. In addition, during tensile testing the lattice rotated toward $\langle 110\rangle$ confirming that shear occurred by the motion of $a/2\langle 110\rangle$ superlattice pairs.

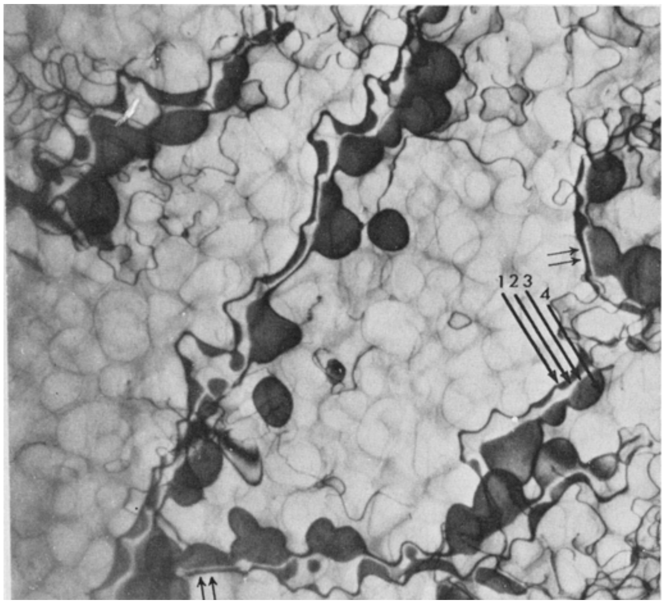

Fig. 7—Transmission micrograph of a section parallel to the critical plane, $(1\bar{1}1)$, showing loosely coupled intrinsic/extrinsic fault pairs in the plane of the foil. Dislocations marked 1 and 4 have $a/3\langle 112\rangle$ Burgers vectors and dislocations 2 and 3 have $a/6\langle 112\rangle$ Burgers vectors. The superlattice intrinsic stacking fault energy was estimated at the locations denoted by the double arrows. Magnification 25,500 times.

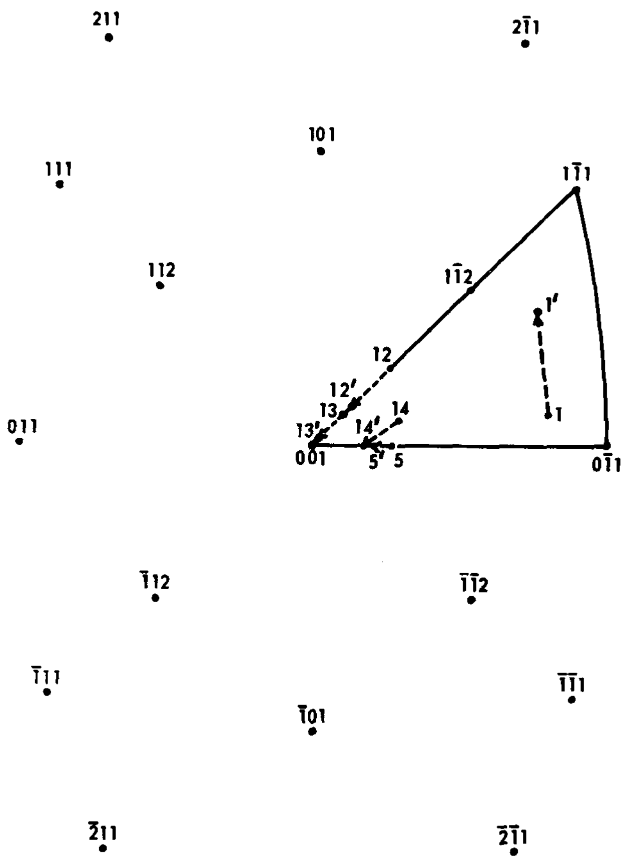

Fig. 8—The rotation of the tensile axes of crystals 1, 5, 12, 13, and 14 during creep deformation. The initial orientation is denoted by the crystal number and the final orientation by the crystal number with a "prime" superscript.

Table IV. Activation Energy for Steady-State Creep

Crystal No.	Temperature Range, °F	Stress, ksi	Activation Energy, kcal per mole
10	1364 to 1410	100	150
7	1365 to 1426	100	150
15	1372 to 1427	85	150
15	1377 to 1401	76.5	143

III) DISCUSSION

A) Incubation Period. Incubation periods have been found in the creep testing of a number of different single crystal materials[21-23] at both high and low temperatures. In general, it would appear that this phenomenon can be attributed to the low grown-in dislocation density found in single crystals and the absence of grain boundaries which commonly act as dislocation sources. In addition, in the case of nickel-base superalloys, a high matrix/particle interaction stress limits the mobility of $a/2\langle 110\rangle$ dislocations until the critical resolved shear stress is reached.[20] This stress is 58 ksi for Mar-M200 at 1400°F, Table V, which is considerably larger than the applied shear stresses on the creep specimens.

Table V. Effect of Prior Creep Deformation on the Critical Resolved Shear Stress for $\{111\}\langle 110\rangle$ Slip

Crystal No.	History	Temperature	Yield Stress, ksi	Schmid Factor	Critical Resolved Shear Stress, ksi
8	Solutionized and aged and crept to 2.7 pct strain at 1400°F and 100 ksi.	1400°F	146.7	0.482	70.6
X5M1	Solutionized and aged.	1400°F	131.5	0.44	57.8
7	Solutionized and aged and crept to 6.3 pct strain at 1365° to 1426°F and 90 to 100 ksi.	R.T.	178.3	0.408	72.8
Y4B4	Solutionized and aged.	R.T.	131.5	0.408	53.6 } Ave: 55.1
X4K4	Solutionized and aged.	R.T.	117.5	0.482	56.6

In order to determine the effect of initial dislocation density on the incubation period, a crystal was loaded at room temperature by a shock wave of 250 kbar intensity, resulting in the introduction of many dislocations as shown in Fig. 9. The initial portion of the creep curve for this crystal at 1400°F and a stress of 100 ksi is shown in Fig. 10. The incubation period was completely eliminated presumably due to the instantaneous generation of $a\langle 112\rangle$ dislocations in the presence of the shock-induced substructure. This supports the idea that the incubation period is caused by a combination of the low initial dislocation density and absence of easily activated dislocation sources.

B) Orientation Dependence of Primary and Steady-State Creep. In order to understand the orientation dependence of the extent and rate of primary creep, one must consider the Schmid factors and multiplicity of slip for $\{111\}\langle 112\rangle$ slip systems. Schmid factor (S.F.) contours in the standard stereographic triangle for the most highly stressed slip systems[24] are shown in Fig. 5(*b*). Several important differences exist between the contours for $\langle 110\rangle$ and $\langle 112\rangle$ slip, as follows:

1) The S.F. for $\langle 112\rangle$ slip is considerably higher for

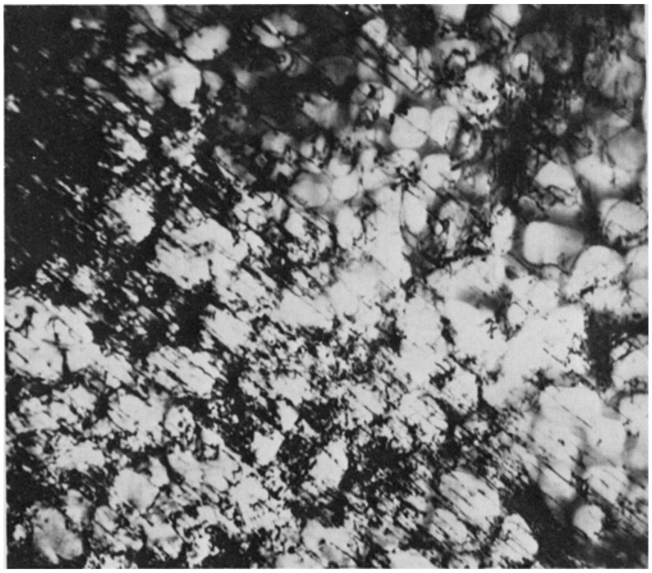

Fig. 9—Transmission micrograph of the dislocation structure introduced by 250 kbar shock wave. Magnification 32,200 times.

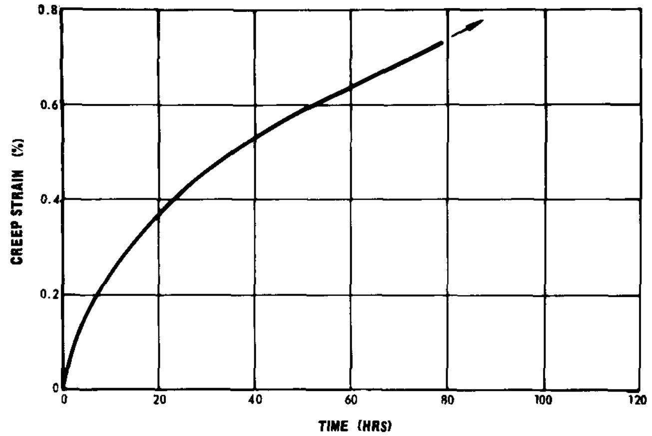

Fig. 10—Initial portion of the creep curve for the shock loaded crystal. Note the absence of the incubation period.

$[001]$, $[0\bar{1}1]$, and $[1\bar{1}1]$ orientations, 3) The primary plane $[\bar{1}\bar{1}1]$ is included in the most highly stressed slip system for all orientations for $\langle 110\rangle$ slip; however, for $\langle 112\rangle$ slip, the critical plane $[1\bar{1}1]$ is most highly stressed in the area $[001]$-X-Y, but the primary plane is most highly stressed in the area Y-$[0\bar{1}1]$-$[1\bar{1}1]$-X; 3) With increasing distance from $[001]$ out to about 20 deg along both the $[001]$-$[0\bar{1}1]$ and $[001]$-$[1\bar{1}1]$ boundary lines as well as between these boundaries, the S.F. increases, passes through a maximum, and then decreases for $\langle 112\rangle$ slip but continually increases for $\langle 110\rangle$ slip; 4) The $[001]$-$[1\bar{1}1]$ boundary line is a symmetry line for $\langle 110\rangle$ duplex slip, but single slip occurs along this boundary between $[001]$ and X for $\langle 112\rangle$ slip.

All the experimental observations of primary creep behavior can now be explained. For example, along the $[001]$-$[0\bar{1}1]$ duplex slip ($(1\bar{1}1)[\bar{1}12]$ and $(\bar{1}\bar{1}1)[112]$) boundary the primary creep rate ($\dot{\epsilon}_p$) and primary creep strain (ϵ_p) for crystals 6, 7, 9, 10, and 8 initially increase, reach a maximum for crystal 10 and then decrease for crystal 8 in accord with the trend in S.F. for the two equally favored slip systems. Crystals 2, 3, 12, 13, and 14 are in single slip orientations, $(1\bar{1}1)[\bar{1}12]$, and exhibit the largest ϵ_p and $\dot{\epsilon}_p$. Crystals 6 and 7 have four equally stressed slip systems, *i.e.*, $(1\bar{1}1)[\bar{1}12]$, $(\bar{1}\bar{1}1)[112]$, $(111)[\bar{1}\bar{1}2]$, and $(\bar{1}11)[1\bar{1}2]$, and exhibit the smallest ϵ_p and $\dot{\epsilon}_p$. The dislocation structure for $[001]$ crystals is shown as a function of strain in primary creep in Fig. 11. It can be seen that strain hardening due to intersecting slip is found at small strains and this, in addition to the relatively low S.F., accounts for the small values of ϵ_p and $\dot{\epsilon}_p$. The effect on the primary creep strain of introducing a high density of dislocations on intersecting slip systems, which limits the mean-free slip distance, is further indicated by the result on the shock loaded crystal, Section IIIA. This crystal had the same orientation as crystal 4, but its primary creep strain was 0.33 pct compared to 3.3 pct for crystal 4. In orientations where strain hardening is not extensive in primary creep, $\dot{\epsilon}_p$ can be predicted analytically.[25]

A measure of the pronounced strain hardening due to intersecting slip, which leads to the transition from primary to steady-state creep, was obtained by performing tensile tests at a strain rate of 2.0 per hr at room temperature and 1400°F on precrept specimens. The critical resolved shear stress for $\{111\}\langle 110\rangle$ slip increased from 55.1 to 72.8 ksi at room temperature and 57.8 to 70.6 ksi at 1400°F, Table V. The strain hardening explains the smaller spread in steady-state creep rates compared to primary creep rates, Section IIA, as a function of orientation. Strain hardening due to multiple slip is always present during steady-state creep, whereas, during primary creep, the strain hardening is large for multiple slip orientations such as $[001]$ but is small for orientations which initially exhibit predominantly single slip.

The importance of developing multiple slip in order to get the transition from primary to steady-state creep is demonstrated by comparing crystals 1 and 12. Both crystals are in single slip orientations. In the case of crystal 1, the S.F. on the most highly stressed slip system, $(\bar{1}\bar{1}1)[2\bar{1}1]$, increased during lattice rotation from an initial value of 0.48 to a maximum of 0.49 and then decreased somewhat to 0.453 at the end of the test. At the same time, the S.F. on the next most highly stressed system, $(1\bar{1}1)[\bar{2}\bar{1}1]$, is initially 0.43 but *decreased* continually during rotation to a final value of 0.25. Therefore, the slip activity on the $(1\bar{1}1)[\bar{2}\bar{1}1]$ system was never sufficient to cause strain hardening and no steady-state creep was observed for this specimen, Fig. 3(*b*). Single slip was further confirmed for this specimen by comparing the calculated elongation for the observed lattice rotation with the actual measured elongation. The calculated and measured values were 34 and 33 pct, respectively. For crystal 12, the most highly stressed system is $(1\bar{1}1)[\bar{1}12]$ and the initial S.F. of 0.48 increased during lattice rotation to 0.5. The next most highly stressed

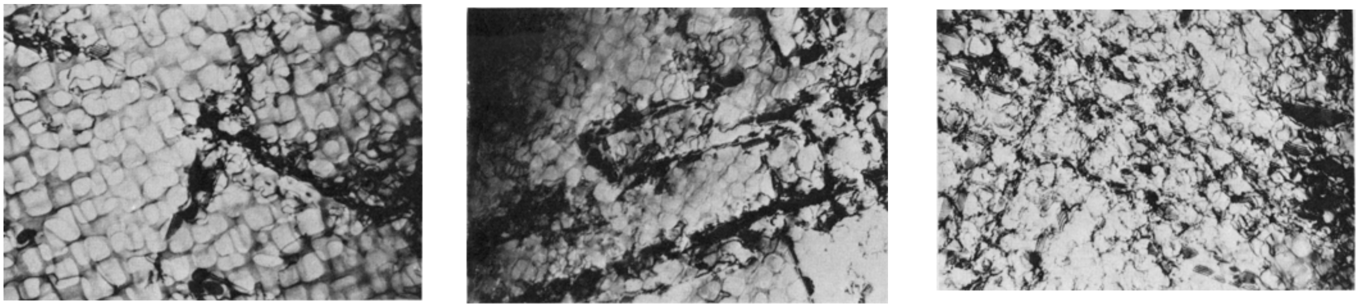
(*a*) (*b*) (*c*)

Fig. 11—Transmission micrographs showing the development of strain hardening (intersecting slip) during primary creep for crystals with a $[001]$ tensile axis; (*a*) 0.35 pct strain, (*b*) 0.80 pct, (*c*) 1.35 pct. Magnification 11,700 times.

slip systems for this orientation are $(\bar{1}\bar{1}1)[112]$ and $(111)[\bar{1}\bar{1}2]$ which initially have S.F.'s of 0.43 and 0.42, respectively. However, during lattice rotation these values *increased* to 0.45 and 0.46 leading to slip activity on these systems and eventual strain hardening. Consequently, steady-state creep was found despite the very large primary creep strain, Table III.

C) The Shear Mode and Rate Controlling Process for Creep. 1) *Primary Creep*. Since the shear of the γ-γ' structure by $a/2\langle 110\rangle$ superlattice pairs requires a larger stress than the applied creep stresses, the substitution of an alternative shear mechanism (intrinsic/extrinsic fault pairs) can be rationalized on this basis. In addition, calculations have indicated[36] that dislocation pairs coupled by intrinsic or extrinsic faults in single phase γ' have a lower total energy than a pair of $a/2\langle 110\rangle$ dislocations separated by antiphase boundary for an APB energy $\geq$150 ergs per sq cm. An estimate of the superlattice intrinsic stacking fault energy was made in areas such as those indicated in Fig. 7 where curvature effects were minimal and therefore neglected. The calculated values ranged from 8 to 17 ergs per sq cm. These values are even lower than those assumed in the analytical treatment,[36] lending further support to the conclusions of the calculation comparing the energies of the two different dislocation arrays.

The motion of the stacking fault pair through the γ' particles is most likely controlled by diffusion (viscous slip) since an adjustment is required at or near the core of the $a/3\langle 112\rangle$ dislocations just as they enter the γ' particles in order to obtain the proper shearing sequence.[17] This explains why this shearing mode is not observed at high strain rates. Viscous slip has previously been proposed for creep of single-phase ordered alloys and compounds.[26,27] The temperature of 1400°F in this investigation is about 0.65 of the solidus temperature and, therefore, diffusional processes should be rapid.

2) *Steady-State Creep*. The interaction between intersecting $\{111\}\langle 112\rangle$ slip systems leads to a steady-state substructure such as that shown in Fig. 12 for crystal 10 at 9.4 pct strain. Dislocation networks have formed at the γ-γ' interfaces and in many cases clearly outline the γ' particles (arrows). Under these circumstances, the mean free slip distance of dislocations is probably on the order of the γ' particle size in contrast to the large distances over which dislocations can glide during primary creep.

The measured activation energy of 150 kcal per mole during steady-state creep was independent of stress which is indicative of a diffusion-controlled creep process,[28] but it is extremely large in magnitude. A similar activation energy was found for the steady-state creep of columnar-grained Mar-M200.[29] Pure nickel[30] has an activation energy for steady-state creep of 66 kcal per mole (equivalent to the activation energy for self-diffusion) and this only increases to 80 kcal per mole with the addition of 30 pct Cr[31] in solid solution. On the other hand, a value of 107 kcal per mole has been found for the creep of Ni_3 (Al,Mo),[32] and comparable values have been determined for other nickel-base superalloys.[5,12] It is possible that the activation energy for diffusion of nickel in the γ' phase is larger than that in disordered nickel alloys as is the case for the diffusion of copper and zinc in ordered and disordered β brass,[33] and experiments are underway to check this point. However, it is questionable whether the activation energy for diffusion is as high as 150 kcal per mole, and, therefore, the possibility that shear of the γ' particles occurs by the same mechanism as in primary creep, but some undefined process at the γ-γ' interface is rate-controlling during steady-state creep cannot be ruled out.

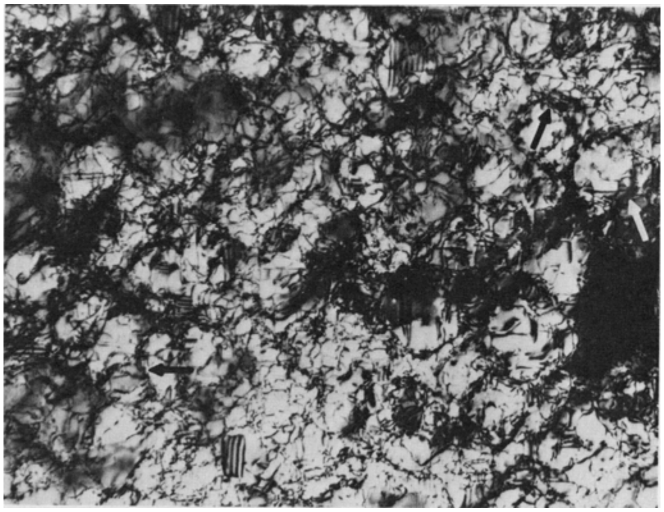

Fig. 12—Transmission micrograph of the steady-state creep substructure in crystal 10 at 9.4 pct strain. Magnification 34,400 times.

D) Implications for Alloy Design. Some generalizations may be drawn from the results of this study relative to the history of the design of nickel-base superalloys. For example, the observation that the γ' particles are sheared during primary creep is a key point. Obviously, if shear of the γ' particles could be avoided by bowing of dislocations between them by the Orowan mechanism,[34] the creep resistance would not be nearly as high, and this is probably the operative creep deformation mechanism, at least during primary creep, in some of the early superalloys that contain low volume fractions of γ'. So, the evolution of alloys with higher aluminum and titanium contents, and consequently with higher volume fractions of γ', can be understood on this basis, and indeed, the most creep resistant alloys such as IN-100 and Mar-M200 have greater than 55 vol pct γ'.[14]

In addition, it can be seen that larger particles would offer more resistance to primary creep deformation than smaller particles for the same volume fraction, since the dislocations tend to conform to the particle shape at the γ-γ' interface, and the restoring force of curved dislocations increases with decreasing radius of curvature. Therefore, penetration of the dislocations into the γ' particles will be easier the smaller the particle radius. Consequently, aging conditions that produce large ($>0.1\ \mu$), *closely spaced* γ' particles should maximize primary creep resistance.

Alloying should affect primary creep behavior in at least two ways. Diffusion rates will be changed by alloying, and certain alloying additions may tend to stabilize stacking faults in the γ' particles which would decrease dislocation mobility. In the case of diffusion, alloying will affect the activation energy for diffusion through its influence on the bond energies between nearest neighbor atoms in the ordered γ' particles and through the size effect on atomic mobility. Stabilization of stacking faults is a special case of the effect of alloying on bond energies and may occur when the faulted stacking sequence corresponds to the crystal structure of the particular alloying addition in combination with nickel. For example, titanium tends to stabilize an extrinsic fault in the $L1_2$ structure (γ') since this fault is equivalent to seven layers of $Ni_3Ti(DO_{24})$.

Steady-state creep resistance depends primarily on having a large volume fraction of γ' particles which can stabilize the dislocation networks formed by intersecting $\{111\}\langle 112\rangle$ slip. The presence of the γ' particles reduces the steady-state creep rate by reducing the rate of recovery. This phenomenon has been observed in other studies at this laboratory and by other investigators.[12] The differences in steady-state creep resistance from one alloy to another will depend on the details of the rate controlling process which is not known at this time. It would be expected, however, that the rate of diffusion and/or the mismatch in lattice parameters at the γ-γ' interface would be important parameters in controlling the creep rate.

Finally, since the Schmid factor for $\langle 112\rangle$ slip is a minimum for a $\langle 111\rangle$ tensile axis and $\langle 111\rangle$ is a multiple-slip orientation, single crystals of this orientation should be most creep-resistant, and evidence exists to support this proposal.[35]

CONCLUSIONS

1) In general, the creep curves of Mar-M200 single crystals at 1400°F are characterized by an incubation period followed by the usual three stages of creep. The incubation period is caused by a combination of the initial low dislocation density, the absence of grain boundary dislocation sources, and the high resistance to glide for dislocations in this material. Multiple slip and subsequent strain hardening are necessary to attain steady-state creep.

2) Creep deformation is homogeneous and occurs by viscous slip of intrinsic/extrinsic fault pairs with net Burgers vector $a\langle 112\rangle$ through both the γ and γ' phases. Intersecting $\{111\}\langle 112\rangle$ slip leads to network formation at the γ-γ' interface during steady-state creep and the activation energy for steady-state creep is 150 kcal per mole.

3) The deformation mode at 1400°F is very sensitive to strain rate. In tensile tests performed at a strain rate of 2.0 per hr, slip occurs in widely-spaced bands by the shear of $a/2\langle 110\rangle$ superlattice pairs through both the γ and γ' phases.

4) The findings for Mar-M200 should be general to all γ' precipitation-hardened nickel-base superalloys where the volume fraction of γ' is large enough to require particle shear during creep and tensile deformation.

ACKNOWLEDGMENTS

The authors would like to acknowledge the contributions of the following people during the course of this investigation: D. Smith and A. D'Acri for creep and tensile testing, J. Hart for specimen and thin foil preparation, and L. Lemaire for operation of the electron microscope.

We also wish to thank Drs. M. Gell and C. H. Wells for valuable criticisms of the manuscript and Drs. A. F. Giamei and J. M. Oblak for stimulating discussions.

REFERENCES

1. W. Betteridge and A. W. Franklin: *J. Inst. Metals,* 1956-57, vol. 85, p. 473.
2. D. McLean: *J. Inst. Metals,* 1956-57, vol. 85, p. 468.
3. C. W. Weaver: *J. Inst. Metals,* 1959-60, vol. 88, p. 296.
4. R. F. Decker, J. P. Rowe, and J. W. Freeman: National Advisory Committee for Aeronautics, Report 1392, 1960.
5. J. Heslop: *J. Inst. Metals,* 1962-63, vol. 91, p. 28.
6. E. L. Raymond: *Trans. TMS-AIME,* 1967, vol. 239, p. 1415.
7. G. A. Webster and B. J. Piearcey: *Trans. Quart. ASM,* 1966, vol. 59, p. 847.
8. G. A. Webster and C. P. Sullivan: *J. Inst. Metals,* 1967, vol. 95, p. 138.
9. P. W. Davies and H. E. Evans: *J. Inst. Metals,* 1968, vol. 96, p. 245.
10. C. P. Sullivan, G. A. Webster, and B. J. Piearcey: *J. Inst. Metals,* 1968, vol. 96, p. 274.
11. P. W. Davies, D. Sidey, and B. Wilshire: *J. Inst. Metals,* 1969, vol. 97, p. 15.
12. D. Sidey and B. Wilshire: *Met. Sci. Jour.,* 1969, vol. 3, p. 56.
13. F. L. VerSnyder, R. B. Barrow, B. J. Piearcey, and L. W. Sink: *Trans. Am. Found. Soc.,* 1969, vol. 55, p. 10.
14. O. H. Kriege and J. M. Baris: *Trans. Quart. ASM,* 1969, vol. 62, p. 195.
15. R. K. Penny, E. G. Ellison, and G. A. Webster: *Mater. Res. Std.,* 1966, vol. 6, p. 76. Also see, D. N. Tishler and C. H. Wells, *Ibid.,* p. 20.
16. B. H. Kear and M. F. Hornbecker: *Trans. Quart. ASM,* 1967, vol. 60, p. 644.
17. B. H. Kear, G. R. Leverant, and J. M. Oblak: *Trns. Quart. ASM,* 1969, vol. 62, p. 639.
18. E. Schmid and W. Boas: *Plasticity of Crystals,* p. 57, F. A. Hughes and Co., London, 1950.
19. H. I. L. Huang, O. D. Sherby, and J. E. Dorn: AIME Trans., 1956, vol. 206, p. 1385.
20. S. M. Copley and B. H. Kear: *Trans. TMS-AIME,* 1967, vol. 239, p. 984.
21. J. B. Wachtman, Jr.: *Creep of Crystalline Nonmetals, Creep and Recovery,* p. 344, ASM, Cleveland, Ohio, 1957.
22. H. L. Burghoff and C. H. Mathewson: *AIME Trans.,* 1941, vol. 143, p. 45.
23. W. G. Johnston: *J. Appl. Phys.,* 1962, vol. 33, p. 2716.
24. E. A. Calnan and C. J. B. Clews: *Phil. Mag.,* 1951, vol. 42, p. 616.
25. P. R. Paslay, C. H. Wells, and G. R. Leverant: Accepted for publication in *J. App. Mech.*
26. J. Weertman: *J. Appl. Phys.,* 1957, vol. 28, p. 1185.
27. J. Weertman: *Trans. TMS-AIME,* 1960, vol. 218, p. 207.
28. F Garofalo: *Fundamentals of Creep and Creep-Rupture in Metals,* The Macmillan Co., p. 91, New York, 1965.
29. G. A. Webster and B. J. Piearcey: *Mat. Sci. Jour.,* 1967, vol. 1, p. 97.
30. J. E. Cannaday, R. J. Austin, and R. K. Saxer: *Trans. TMS-AIME,* 1966, vol. 236, p. 595.
31. J. P. Dennison, R. J. Llewellyn, and B. Wilshire: *J. Inst. Metals,* 1967, vol. 95, p. 115.
32. G. R. Leverant and D. N. Duhl: unpublished research, Pratt and Whitney Aircraft, Middletown, Conn., 1968.
33. A. B. Kuper, D. Lazarus, J. R. Manning, and C. T. Tomizuka: *J. Appl. Phys.,* 1956, vol. 104, p. 1536.
34. E. Orowan: *Symposium on Internal Stresses in Metals and Alloys,* p. 451, Inst. Met., London, 1948.
35. B. H. Kear and B. J. Piearcey: *Trans. TMS-AIME,* 1967, vol. 239, p. 1209.
36. A. Giamei and B. H. Kear: unpublished research, Pratt and Whitney Aircaraft, Middletown, Conn., 1969.